Mon. Not. R. Astron. Soc. 000, 1–13 (2001) Printed 29 August 2005 (MN LaTeX style file v1.4)

Surveying the Sky with the Arcminute MicroKelvin Imager: Expected Constraints on Galaxy Cluster Evolution and Cosmology

Rüdiger Kneissl[1], Michael E. Jones[1], Richard Saunders[1], Vincent R. Eke[2,3], Anthony N. Lasenby[1], Keith Grainge[1] and Garret Cotter[1]
[1] *Astrophysics, Cavendish Laboratory, Cambridge University, Madingley Road, Cambridge CB3 0HE, UK*
[2] *Institute of Astronomy, Cambridge University, Madingley Road, Cambridge CB3 0HA, UK*
[3] *Steward Observatory, 933 N Cherry Ave, Tucson AZ 85721, USA*

arXiv:astro-ph/0103042 v2 6 Mar 2001

Accepted Received In original form

ABSTRACT

We discuss prospects for cluster detection via the Sunyaev-Zel'dovich (SZ) effect in a blank field survey with the proposed interferometer array, the Arcminute MicroKelvin Imager (AMI). Clusters of galaxies selected in the SZ effect probe cosmology and structure formation with little observational bias, because the effect directly measures integrated gas pressure, and does so independently of cluster redshift.

We use hydrodynamical simulations in combination with the Press-Schechter expression to simulate SZ cluster sky maps. These are used with simulations of the observation process to gauge the expected SZ cluster counts. Even with a very conservative choice of parameters we find that AMI will discover at least several tens of clusters every year with $M_{\rm tot} \geq 10^{14} M_{\odot}$; the numbers depend on factors such as the mean matter density, the density fluctuation power spectrum and cluster gas evolution. The AMI survey itself can distinguish between these to some degree, and parameter degeneracies are largely eliminated given optical and X-ray follow-up of these clusters; this will also permit direct investigation of cluster physics and what drives the evolution.

Key words: cosmology:observations – cosmic microwave background – galaxies:clusters:general

1 INTRODUCTION

Clusters of galaxies are the most massive collapsed objects in the universe. They are ideal probes of structure formation, both in the linear clustering regime, which is controlled by factors such as the cosmological density parameter Ω_0 and the density fluctuation power spectrum, and later when the individual clusters grow non-linearly by merging, shocks, and gradual virialisation. It is becoming clear that there is a population of clusters $z \geq 1$ (see e.g. Fabian et al. 2001, Cotter et al., Joy et al.), but the numbers of these remain unclear. It is essential to search systematically for these clusters in order to understand the evolution of structure in the universe.

To make full use of these probes of cosmology, an unbiased cluster survey is needed. Optical and X-ray surveys suffer various biases with respect to cluster properties and redshift. Projection effects, confusion with background objects, surface brightness dimming with redshift, and a bias to mass concentration, all hamper both optical and X-ray surveys, although X-ray luminosity turns out to be a reasonably good indicator of the total mass in many clusters. However, detecting clusters via the scattering of CMB photons by cluster gas (the Sunyaev–Zel'dovich, SZ, effect, Sunyaev & Zel'dovich 1972) minimises such biases.

First, the measured quantity, integrated gas pressure, gas mass times gas temperature, or total thermal energy is closely related to the cluster mass (e.g. Bartlett and Silk 1994; Barbosa et al. 1996; Eke et al. 1996). Second, critically, because the SZ effect is a scattering process, the effect is independent of cluster redshift. Surveys using the SZ effect therefore offer the means to find clusters by mass, and at all redshifts.

Detection of the SZ effect in rich X-ray-selected clusters has become routine (see Birkinshaw 1999 for a review) Although the use of microwave cluster searches for cosmological studies has be advocated for a long time (Korolev, Sunyaev & Yakubtsev 1986; Bond & Myers 1991; Bartlett &

© 2001 RAS

Silk 1994; Markevitch et al. 1994; Barbosa et al. 1996; Eke et al. 1996; Colafrancesco et al. 1997; da Silva et al. 2000) only very recently has the technology and expertise become available to build sufficiently sensitive instruments that can survey the sky and are expected to find a substantial number of clusters in a reasonable surveying time.

In this paper we will explore the expected results from an SZ survey using the characteristics of the proposed Arcminute MicroKelvin Imager (AMI). Other related experiments are proposed or planned (SZA: Holder et al. 2000, AMiBA: Lo et al.). Predictions for the results of this kind of survey exist now also in the literature (e.g. Holder et al. 2000, Bartlett). The work presented here (cf. Kneissl 2000 for an earlier presentation) is different in two main ways:

- We have tried to be as conservative as possible about what an AMI survey will find, given what is already known about structure formation. For example, Holder et al. (entirely reasonably) expect to find larger numbers of clusters than we report here; however, this difference is only due to their different choice of model parameters: f_g (gas fraction) higher by 50% and σ_8 (rms density fluctuations on 8 Mpc scales) higher by 20%. This change in the parameters leads to a number of clusters that is higher by a factor of ten. This large difference in expected source counts for a plausible variation in input parameters clearly demonstrates the importance of observations which will have an error of the order of only about 10%. Since the uncertainties in the model parameters entering the SZ cluster simulation are large, we take a cautious approach and demonstrate that Ω_0 can be sensibly constrained even with a pessimistic parameter choice. With more optimistic assumptions for the model parameters, in particular the gas fraction and the local cluster abundance, more clusters are expected, and higher precision in constraining parameters can be achieved. Constraints on a cosmological constant or even quintessence (Wang and Steinhardt 1998, Haiman et al.) are possible in principle and are certainly a fascinating possibility. Also deviations from the expected gravitational evolution allows us to identify non-Gaussian initial conditions (e.g. Matarrese et al. 2000).
- We model what *interferometers* will detect, given their uv coverage, their errors, and given the ubiquitous existence of contaminating radio sources.

AMI is described and a brief overview over its other science goals is given in Section 2. To gauge the ability of AMI to detect clusters, we simulate the SZ cluster sky using the Press-Schechter expression and individual cluster templates from hydrodynamical simulations, described in Section 3. The expected cluster counts and instrument sensitivities are considered in Section 4, and in Section 5 we discuss the exciting prospects of using AMI results to determine the model parameters, and follow-up observations, both pointed SZ observations and in other wavebands. We argue that detection in the SZ effect is vital for selection, and follow-up in the optical and X-ray bands is necessary to break degeneracies between the model parameters.

2 THE ARCMINUTE MICROKELVIN IMAGER

It has not yet proved possible to conduct an effective blind SZ survey because of the limited sensitivity and field of view of current telescopes. A very rich cluster produces a perturbation of less than 1 mK on the CMB, over an angular size (for a moderate-to-high redshift cluster) of a few arcminutes. A small number of groups have been able to detect successfully the SZ effect in X-ray and optically selected clusters (e.g. Birkinshaw, Gull & Hardebeck 1984; Jones et al. 1993; Carlstrom, Joy & Grego 1996; Holzapfel et al. 1997; Myers et al. 1997). However, existing telescopes do not have sufficient sensitivity over a large enough field of view to carry out a survey that would usefully constrain the population of clusters at high redshifts where X-ray and optical surveys are incomplete.

As an example, our present programme uses the Ryle Telescope (RT) at 15 GHz to make images of the SZ effect in X-ray selected clusters. The RT, with its compact array of five 13 m-diameter antennas, was the first instrument in practice capable of imaging the SZ effect, and remains one of only a handful of such worldwide. We have obtained $\sim$10-σ detections towards a dozen clusters (see e.g. (Grainge et al. 1993; Grainge et al. 1996)). However, it takes about twenty 12-hour observations with the RT to achieve a 5-σ detection on a rich (total mass $\approx 10^{15}\mathrm{M}_{\odot}, kT \approx 8\mathrm{keV}$) cluster, with a field of view of 0.01 square degrees. Models of structure formation normalised to the local space density of clusters e.g. (Eke, Cole, & Frenk 1996) suggest that the surface density of such clusters is at most of the order 0.1 per square degree. Thus to detect a few such clusters with the RT in a blind survey would take over fifty years.

Given the experience of existing SZ and CMB telescopes, it is now possible to build an SZ survey telescope with the required performance. Interferometers have advantages over single antennas for the kind of measurements we need to make. They are less susceptible to spillover signals in the sidelobes, as signals originating far from the main beam are attenuated both by delay error and by having the wrong fringe rate. Receiver stability is not critical as gain fluctuations are not correlated between different antennas and are therefore not coherently detected by the correlator. They can be very insensitive to most atmospheric emission, both by resolving it out spatially, and by virtue of the fact that it has a very different fringe rate to the astronomical signal and can be filtered out temporally (Church 1995; Lay & Halverson 2000). With suitable design, interferometers can also overcome the ever-present problem of radio sources contaminating the CMB signal by simultaneously identifying the sources with high angular resolution and subtracting them from the short-baseline data.

The design of an SZ survey interferometer has to address two basic issues:

- Good temperature sensitivity is required: we must maintain a high filled fraction of the synthesised aperture yet have a sufficient range of baselines to make a good image. Also we must not resolve out the extended structure of most SZ sources – their typical angular size of a few arcminutes requires baselines of a few hundred wavelengths or less in order to observe most of the flux. We therefore need a closely-packed array of small antennas.

- It is also vital to find and remove the effects of contaminating foreground emission. In practice on arcminute scales, the contamination comes from discrete point sources—radio galaxies and quasars. Their effects can only be removed by mapping the AMI field of view with higher angular resolution and flux sensitivity. This requires an array of large antennas with relatively long baselines.

The solution to these problems is to use two arrays simultaneously; larger antennas on longer baselines, providing good flux sensitivity to point sources, and a compact array of small antennas to provide sensitivity to the SZ clusters. For AMI, we propose to use all eight 13-m antennas of the RT, with baselines from 18 to 108 m (900 to 5400 λ at 15 GHz), plus a new array of ten 3.7-m antennas with baselines from 4 to 18 m (200 to 900 λ). The 3.7-m antennas will be sited inside an earth bank lined with aluminium sheeting to ensure that sidelobes from the antennas do not terminate on warm emitting material (see figure 1). The filling factor is around 40% for baselines up to $\sim 2000\lambda$, giving good temperature sensitivity with a resolution of 1.5 arcmin. The shorter baselines of the RT array provide some sensitivity to SZ clusters; the remaining longer baselines provide sufficient flux sensitivity at higher resolution to subtract the radio sources that will also be present in any field. We will correlate the whole 12–18 GHz band provided by the front-end amplifiers, divided into 8 channels (or 16 in the case of the longer RT baselines) to avoid losses due to chromatic aberration.

We choose the 12–18 GHz band for several reasons. At a given resolution and system temperature, any observing frequency within the Rayleigh-Jeans region of the CMB spectrum ($\nu \ll 217$ GHz) will give the same sensitivity to temperature structure in the sky. The relevant questions are then of achievable system temperature and foreground contamination. Receiver noises are invariably lower at lower frequency; modern cryogenic amplifiers using pseudomorphic HEMTs can achieve noise temperatures of 0.5–1 K per GHz of observing frequency at $\nu < 150$ GHz. Also, the atmospheric noise contribution rises with frequency and is more sensitive to the water vapour content at higher frequencies. On the other hand, the major foreground contaminant at arcminute resolution is extragalactic radio sources, whose brightness temperature typically falls as ν^{-2} to ν^{-3}. (Note however that Taylor et al., using the RT at 15 GHz in survey mode, find a significant population of sources whose flux densities *rise* with frequency, i.e. whose brightness temperatures fall more slowly than ν^{-2}.) Optimum observing frequency is thus a compromise between system noise and source contamination. With the RT, a large collecting area is available for source identification on a site where the atmosphere is very much more transparent at 12–18 GHz than at the next atmospheric window of 26–36 GHz. System temperatures around 25 K are possible using the latest amplifiers, and the source confusion problem is quite tractable using the majority of the RT baselines. Observing solely in the Rayleigh-Jeans region means of course we are unable to use the frequency dependence of the SZ effect to separate the thermal and kinetic SZ effects; however, for the main purpose of making an SZ survey, sensitivity is the over-riding consideration, and this is best achieved at lower frequency.

Figure 1. The Arcminute MicroKelvin Imager is planned to consist of eight 13-m dishes of the Ryle telescope, five of which are visible in the top image, and an array of 3.7-m antennas, which can be seen in the artist's impression below.

2.1 Predicted Performance

The instantaneous field of view, or primary beam, of an interferometer is given by the Fourier transform of the antenna illumination function; for typical illumination patterns, the field is well approximated by a Gaussian with FWHM $= 1.1\lambda/D$ where D is the antenna diameter. The flux sensitivity of an array consisting of n antennas each with effective area A, integrating for a time τ, measuring a single polarisation with bandwidth $\Delta\nu$ is given by (see e.g. Thomson, Moran & Swenson 1986)

$$\Delta S_{\rm rms} = \frac{2kT_{sys}}{\eta A \left(n\left(n-1\right)\Delta\nu\ \tau\right)^{1/2}},$$

where η is the system efficiency, T_{sys} is the system temperature (assumed the same for each antenna), and k is Boltzmann's constant. For the two arrays of AMI, this results in flux sensitivities of $2.0 \mathrm{mJy\,s^{-1/2}}$ and $20 \mathrm{mJy\,s^{-1/2}}$ over fields of view of 6 arcmin and 21 arcmin respectively. These figures have been used to generate the sensitivity plots and simulated observations in the following sections. To give an indication of the equivalent temperature sensitivity, we assume that the aperture is reasonably well-filled and use the

Rayleigh–Jeans formula. This gives

$$\Delta T_{\rm rms} = \frac{\lambda^2 \Delta S_{\rm rms}}{2k\Omega},$$

where Ω is the synthesised beam area. This corresponds to a temperature sensitivity of around 8 μK in a 1.5 arcminute beam in one month of observation on a single (0.1 square degree) field, though sensitivity can be concentrated on particular angular scales by choice of array configuration.

2.2 Source subtraction

We now show that AMI can successfully subtract the radio sources that are the main contaminating signal. The amount of collecting area that has to be devoted to source subtraction depends critically on the source counts at the flux levels being probed. There are no good deep source counts available at 15 GHz; however there exist μJy source counts at 8.4 GHz, less than a factor of two in frequency away from where AMI would operate, allowing us to assess roughly the level of source confusion. Windhorst et al (1993) find the 8.4 GHz source counts below 1 mJy are described by

$$N(>S) = (3.57 \pm .57)\,(S_{8.4}/1\,{\rm Jy})^{-1.3\pm0.2}\ {\rm sr}^{-1}.$$

Using the effective spectral index of $\alpha = 0.53$ (taking into account the dispersion in their measured spectral indices), extrapolation to 15 GHz gives

$$N(>S) = 2.6\,(S_{15}/1\,{\rm Jy})^{-1.3}\ {\rm sr}^{-1}.$$

To calculate the effect of source confusion on AMI, we split the baselines into two sets. The first is dedicated to high temperature sensitivity mapping of arc-minute scale CMB structure, and so comprises only baselines shorter than 2 kλ; these are all 45 baselines from the 3.7-m antennas and 6 baselines between the 13-m antennas. This set has a flux sensitivity of 51 μJy (12 hours)$^{-1/2}$ over a 0.1 square degree field. The second measures the flux densities of confusing radio sources and comprises the remaining 22 baselines from the 13-m antennas. It has a flux sensitivity of 35 μJy over the same area in the same time. The residual confusion noise in the maps made with the compact set is given by

$$\sigma^2_{\rm conf} = \Omega \int_0^{S_{\rm sub}} S^2 \frac{{\rm d}N}{{\rm d}S}{\rm d}S,$$

where Ω is the synthesised beam area and $S_{\rm sub}$ is the flux level subtracted down to. Assuming a source detection threshold (4.0σ) of 140 μJy, we find that the residual confusion noise in a 12-hour, 1.5-arcmin resolution AMI observation is 30μJy, which when added in quadrature to the thermal noise results in a less than 20% increase in overall noise level. In practice, simultaneous fitting of the clusters and point sources to all the baselines will increase the effective sensitivity to sources and allow them to be subtracted to an even lower level.

This design achieves optimal sensitivity to the cluster SZ effect and a separation with other components such as radio sources. Although a main aim is the study of clusters, it will probe generally the structure of the CMB on scales smaller than those accessible to the Planck satellite. It is sensitive to phenomena such as inhomogeneous ionisation, density–velocity correlations (Ostriker-Vishniac effect), filaments and topological defects, which are all of immense interest as well. In the following sections, however, we demonstrate the ability of AMI to discover clusters.

3 SIMULATED SZ CLUSTER SKY MAPS

To determine how many galaxy clusters AMI might detect, it is useful to create realistic SZ sky maps simulated for different cosmologies. This approach is particularly helpful for interferometric measurements for the following two reasons. Firstly, limited coverage in the aperture (uv) plane produces ringing in real space, where clusters are most easily identified. Thus, the resulting point-source response in the interferometer observation, the synthesised beam, has a complicated wing structure that produces correlated noise. The extent to which this impacts upon the cluster detection efficiency is difficult to gauge without simulations of the instrumental response applied to realistic input sky maps. Secondly, because interferometers are sensitive to the detailed shapes of the structures they observe, it is important that the simulated clusters should have a realistic distribution of shapes and sizes.

Two extreme cases of cluster evolution are considered here by assuming a flat and an open universe with $\Omega_0 = 1$ and 0.3 respectively. The inclusion of a Λ–like term does not greatly change the cluster number counts (eg. Eke, Cole & Frenk 1996), so this complication is not introduced into the models. A Hubble constant of 70 km s^{-1} Mpc^{-1} is chosen for both cases, and the assumed cold dark matter power spectrum of density fluctuations is described by a shape $\Gamma = 0.25$ (Bardeen et al. 1986) and a linear theory rms amplitude of mass fluctuations matching the present-day cluster abundance as given by

$$\sigma_8 = (0.52 \pm 0.04)\,\Omega_0^{-0.46+0.10\,\Omega_0}, \qquad (1)$$

(Eke et al. 1996).

The above parameters define the background cosmological models and the dark matter properties. In order to create SZ sky maps, it is also necessary to specify the fraction f_g of mass that is in the intracluster gas, and the conversion between total cluster mass and gas temperature as parametrised by β in

$$\frac{kT_{gas}}{\rm keV} = \frac{7.75}{\beta}\left(\frac{M}{10^{15}h^{-1}{\rm M}_\odot}\right)^{\frac{2}{3}}\left(\frac{\Omega_0}{\Omega(z)}\right)^{\frac{1}{3}}\left(\frac{\Delta_c}{178}\right)^{\frac{1}{3}}(1+z). \qquad (2)$$

M represents the cluster virial mass and Δ_c is the ratio of mean halo density to critical density at the redshift of observation, $z$in a spherical collapse model. As the electron density in the intracluster gas is proportional to f_g, and the cluster SZ decrement is proportional to the integrated line-of-sight electron pressure, the choice of f_g/β has a significant impact upon the anticipated signals from the clusters. While the value of β can be estimated as $\beta \approx 1$, the value adopted here, to an accuracy of the order of 10 % from hydrodynamical simulations (Bryan & Norman 1998), there is a somewhat larger uncertainty in f_g. If one chooses to set f_g using the measured intracluster gas fractions, then the value should lie in the range given by Ettori and Fabian (1999) and

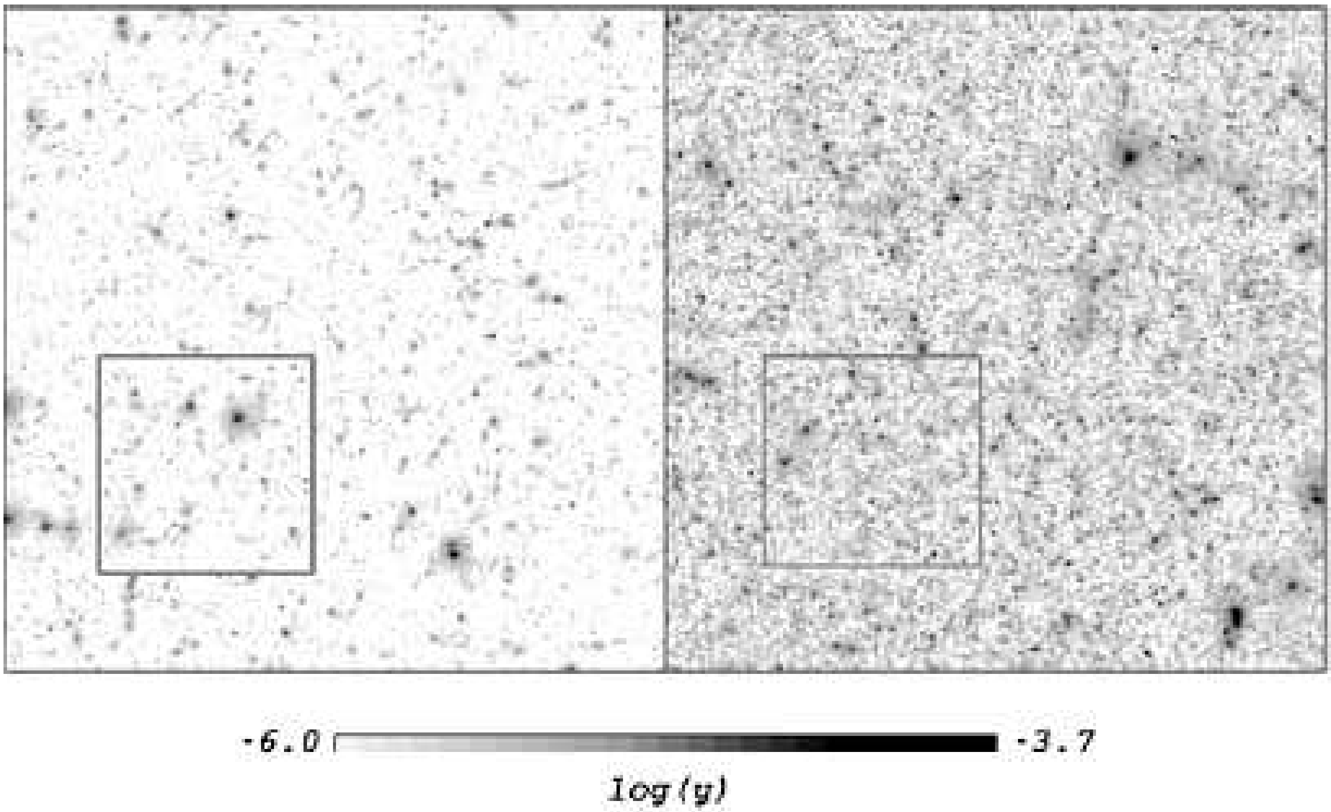

Figure 2. SZ cluster maps (0.75 arcmin pixels, $5° \times 5°$), simulated as described in the text, with $\Omega_0 = 1$ (left) and $\Omega_0 = 0.3$ (right). AMI observations of the framed fields have been simulated in detail and are presented in Figure 6.

Mohr, Mathiesen and Evrard (1999), who both find 0.1–0.25 at the 95 % confidence level. An alternative way to choose f_g would be through the primordial nucleosynthesis value for the fraction of the critical density contributed by baryons, $\Omega_b \approx 0.019\, h^{-2} \approx 0.04$ (Tytler et al. 2000). For the two different Ω_0 values, the assumptions that clusters contain the universal baryon fraction (White et al. 1993) and that all baryons are in the gaseous component lead to $f_g = 0.04$ and 0.13. A value of $f_g = 0.1$ has been used for both maps described in this paper. This is on the low side unless Ω equals 1, and primordial nucleosynthesis is a more appropriate way to determine f_g than studying clusters themselves. Thus, the predicted cluster number counts are likely to be lower than might otherwise be expected. Furthermore, the choice of the same f_g for both cosmologies will reduce the difference between the total numbers of detectable sources relative to what would be found with f_g inferred from nucleosynthesis. The model parameters are summarized in Table 1.

Ω_0	1.0	0.3
h	0.7	0.7
σ_8	0.52	0.87
Γ	0.25	0.25
f_g	0.1	0.1
β	1	1
X	0.76	0.76
$(\Omega_{\rm b} h^2$	.049	.0147)

Table 1. Summary of model parameters. The universal gas fraction is $f_g = m_b/m_{DM}$, $\beta = \mu m \sigma^2/kT$ is the ratio of kinetic to thermal energy in the cluster gas, and $X = m_{\rm H}/m_{\rm total}$ the hydrogen / helium ratio.

To produce a map, the Press-Schechter expression (1974) is used to create a list of cluster masses and redshifts. The centres of these clusters are placed at random within a $5° \times 5°$ sky map with 45 arcsec pixels, and template cluster maps are pasted, suitably scaled, onto these positions. Individual cluster templates are produced from the ten ΛCDM hydrodynamical cluster simulations of Eke, Navarro and Frenk (1998). Each cluster is observed at eight different redshifts out to $z \approx 1.1$, and templates are produced from three orthogonal directions to maximise the variety in the apparent cluster shapes. At $z = 0$ these clusters have total masses of $\sim 10^{15} M_\odot$ and thus represent the largest virialised structures. If a smaller cluster is required then the templates are scaled down in angular size, gas temperature and SZ emission accordingly. The discrete redshift sampling of the simulations means that some scaling of the template emission to the desired redshift is also necessary. The two simulated SZ maps are shown in Figure 2.

da Silva et al. (2000) simulated SZ sky maps by stacking together hydrodynamical simulation boxes, in order to gain sufficient depth in redshift. Once the different choices of the various parameters that are described above are taken into account, σ_8 being of particular importance, their mean flux decrement per pixel is $\approx 30\%$ greater than that found in the maps produced here. Decreasing the minimum SZ flux of the included clusters from $Y_{min} = 4 \times 10^{-7} h$ arcmin^2 largely

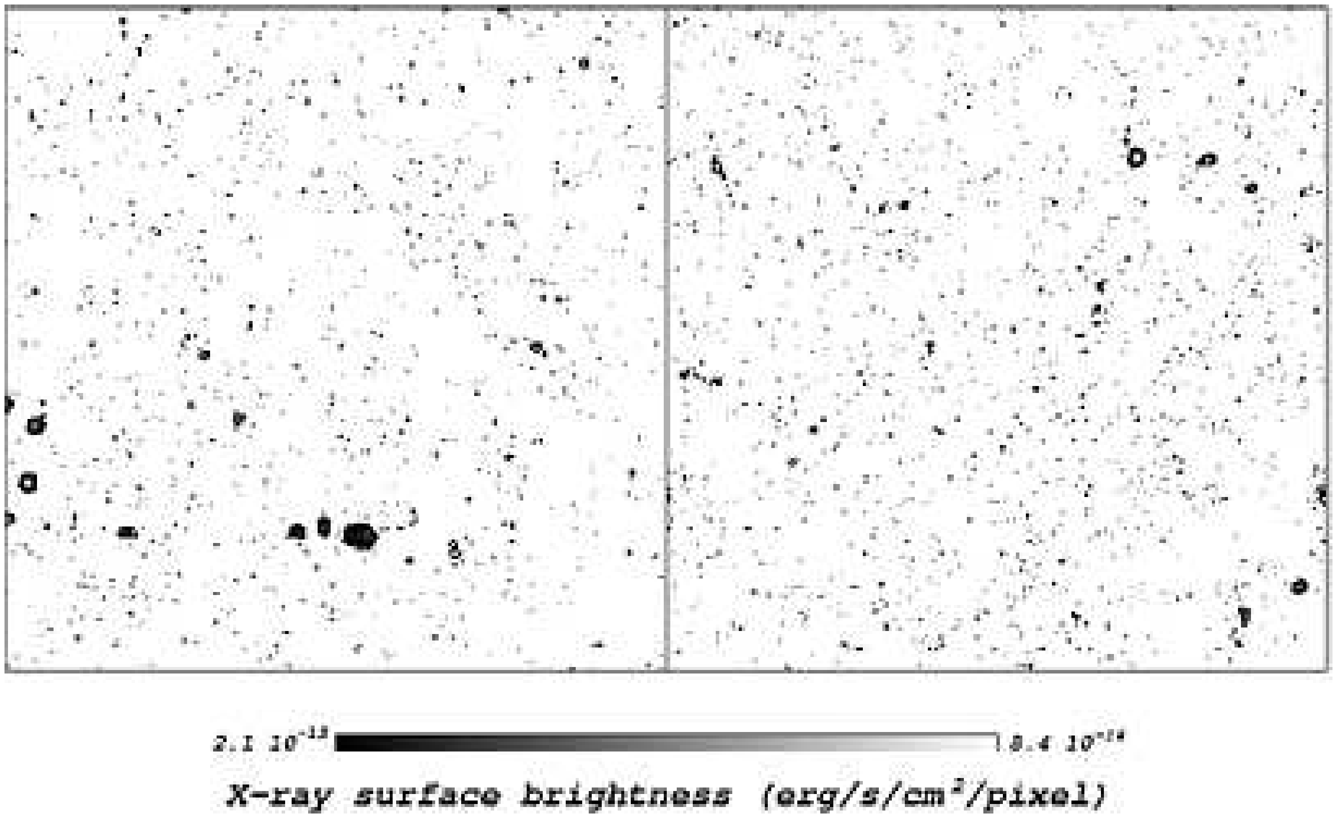

Figure 3. The 0.5–2 keV X-ray corresponding to Figure 2. The X-ray surface brightness limits of the greyscale bar (2.1×10^{-15};8.4×10^{-14}) correspond to 0.1 and 2.5×10^{-3} XMM-Newton (EPIC) counts s^{-1} and per (0.56 arcmin^2) pixel. The lower limit corresponds to the sensitivity of a medium-deep XMM survey. Note that the grayscale is inverted against the background to enhance the contrast. Only a minimal difference between the cosmologies ($\Omega_0 = 1$ to the left and $\Omega_0 = 0.3$ to the right) is visible even at this low surface brightness limit, because the redshift selection (see Figure 13) is so different to the SZ effect.

accounts for the difference in mean flux. Y is the integral of the Compton y parameter over the cluster solid angle (ie area divided by the angular diameter distance squared, $Y = r_d^{-2} \int y \, \mathrm{d}A$). However, this difference is less than 10 % of the flux of the faintest detected clusters, so this does not significantly influence the number of clusters that are detected here.

X-ray cluster emission templates were also produced using the same simulated hydrodynamical clusters as for the SZ templates. Bolometric luminosities were calculated from the particle densities and temperatures according to equation (15) of Eke et al. (1998). This allowed the corresponding X-ray maps to be created, so that the same simulated skies could be observed at other wavelengths. 0.5–2 keV and 2-10 keV maps were created, with the cluster luminosities being scaled from the template temperature to that of the required cluster assuming the non-evolving

$$L_x \propto T^3 \qquad (3)$$

(Ettori, Allen & Fabian 2001, Donahue et al. 1999, Della Ceca et al. 2000, Schindler 1999, Fabian et al. 2001), rather than the $L_x \propto T^2(1+z)^{3/2}$ that is expected from simple scaling arguments. Possible evolution affects our modelling only very weakly, since we rescale within a redshift bin. The 0.5-2 keV X-ray cluster map is complete to an X-ray flux limit of 1×10^{-15} erg cm^{-2} s^{-1}.

4 DETECTING CLUSTERS WITH AMI

We simulate the cluster detection process for a blank field AMI observation in two different ways: a detailed, but time consuming, simulation of the response of the interferometric array to the structure on the sky, and a simplified simulation, which only operates in the image plane and uses a compensated beam profile that is constructed to match the synthesized beam resulting from the more detailed simulations.

The simplified procedure, aims at determining the cluster counts resulting from mosaiced observations, and with a realistic beam, in a fast and straightforward way. The synthesised beam depends on the coverage in the visibility plane which itself depends on the array configuration, the sky position of the field and the length of observations. The finiteness of the coverage causes ringing in the Fourier transform and the wing-structure of the beam. An accurate analytic description can be given with Bessel functions, which however still requires knowledge of the visibility coverage and substantial computational efforts. However a simpler model for the beam with only a few parameters can be given by a Gaussian beam with a compensating negative ring (see Figure 4), which approximates the most relevant parts of the synthesised beam surprisingly well. Convolving the simulated SZ cluster map with this beam results in a map in

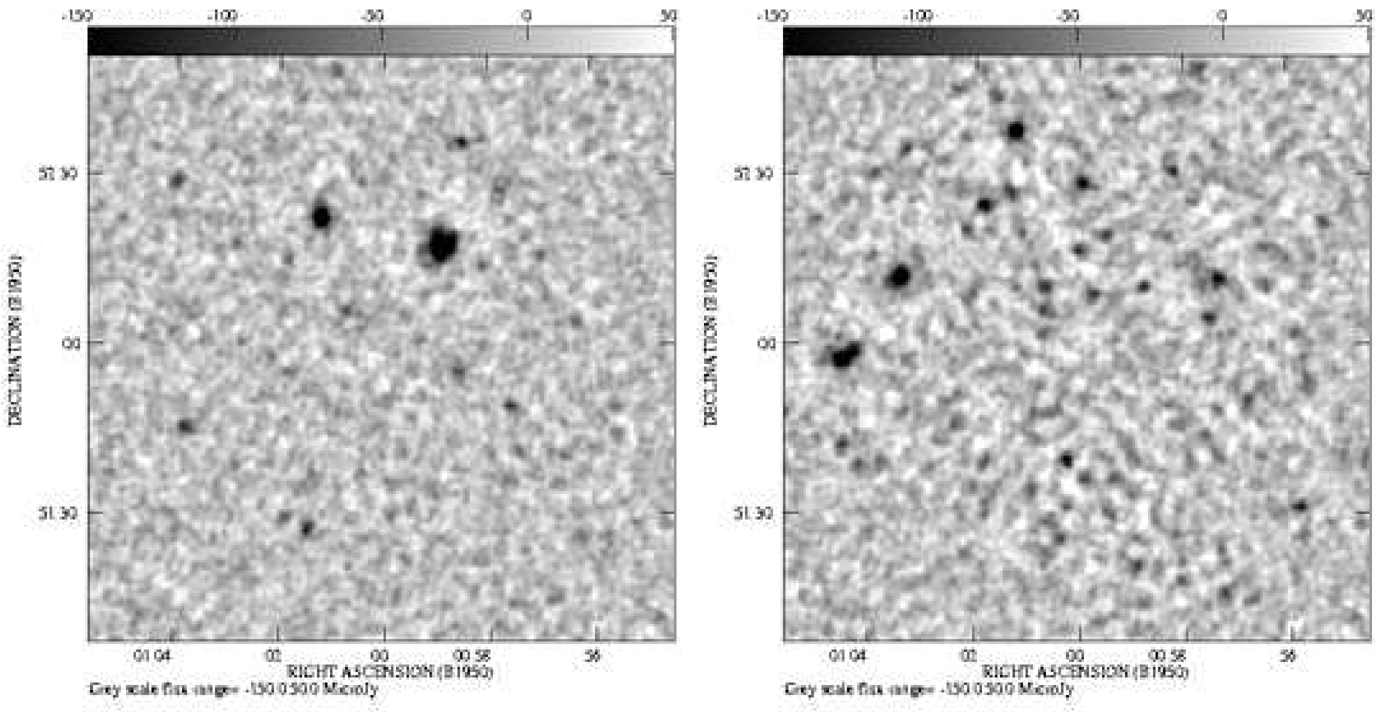

Figure 6. Two simulated AMI observations of 20-arcmin radius fields showing the effects of the different cosmologies ($\Omega_0 = 1$ on the left and $\Omega_0 = 0.3$ on the right; units are μJy beam^{-1}. The clusters show as dark (negative) features against the CMB. The simulation with low matter density has many more moderate mass clusters, because clusters form early and we can see them in SZ all the way to very high redshift.

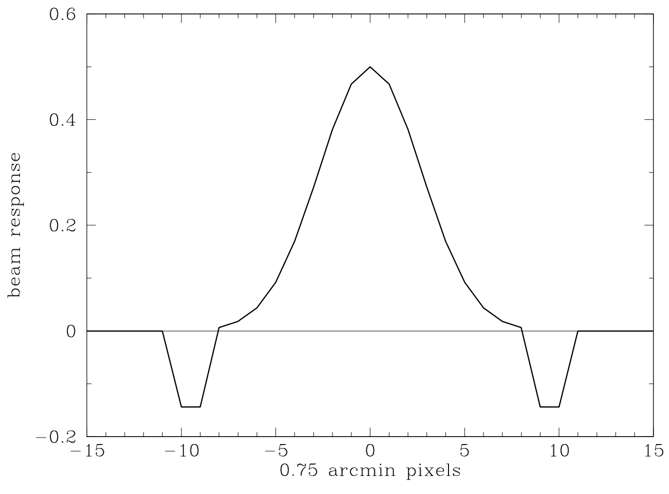

Figure 4. A model for the synthesised beam of AMI. The beam efficiency, central height, is 0.5, FWHM is 4.8 arcmin and the only other two parameters, since the beam is exactly compensated, the inner and outer radii of the ring are adjusted to be at 3 and 4 σ of the Gaussian (6.12 and 8.16 arcmin) respectively. When this beam model is convolved with a typical cluster profile it gives a good approximation to the flux observed in the detailed simulations (Figure 7).

which the brighter pixels give the positions and fluxes of the brightest clusters; others can be confused.

After convolution of the cluster sky maps with this beam the observed cluster fluxes and the integrated cluster counts can be constructed (see Figure 5). Here a beam width of 4.5 arcmin FWHM and a beam efficiency of 0.5 were assumed. In addition to the recovered cluster counts we show the 1-σ and 4-σ sensitivity lines for various observation times. We assume a Gaussian thermal noise floor corresponding to a system temperature of 30 K.

The detailed telescope model takes all baselines of a given array configuration, and calculates the uv coverage for an observing run. The simulated sky images are multiplied by the interferometer primary beam, Fourier transformed, and then sampled at the calculated positions in the uv plane. Gaussian noise is added to the data points at the appropriate level. The resulting 'observed' data are then used to produce a map (see Figure 6 for an example) in the same way real observations are analysed, i.e. with AIPS tasks, and the detected clusters are extracted from the CLEANed map. We compare the cluster fluxes so derived with those from the fast procedure (see Figure 7) and find variations and scatter between the two methods that are small in relation to the uncertainties in the cluster sky model parameters. We conclude that the predicted cluster counts are not affected by these differences.

5 DETERMINATION OF MODEL PARAMETERS

5.1 Based on AMI cluster counts

After one year of observation AMI will have completed an unbiased cluster survey down to roughly 10^{14} $M_\odot$ with 20 ($\Omega_0 = 1$) to 70 ($\Omega_0 = 0.3$) clusters for our pessimistic as-

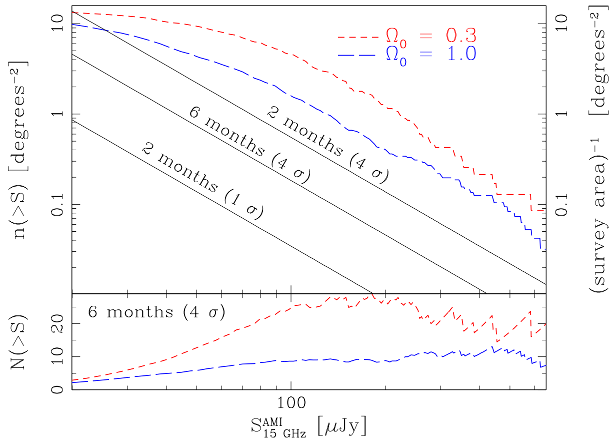

Figure 5. Upper panel: Observed AMI SZ cluster cluster source counts for low (short dashed; top) and high (long dashed; below) matter density and survey sensitivity lines (solid; labeled) in (sky area)$^{-1}$ as a function of observation time. The ratio between these curves equals the number of detected clusters (lower panel). At high fluxes the cluster counts rise steeper than the sensitivity lines, showing that a deeper survey will return more clusters for the same observation time up to the point where confusion sets in. Thus a broad maximum in the expected number of clusters is seen at around a few hundred μJy for both cosmologies. However the cluster counts can also be tested with good efficiency over a wide range of fluxes by surveying differing areas at appropriate depths. Note that a shift in the position of the maximum to lower fluxes with decreasing matter density is in fact expected, since the increasing number of high redshift clusters steepens the cluster counts which are normalised at high fluxes (cf. Figure 9). The error on the ratio of the curves and the field-to-field variation is approximated well by Poisson statistics for cluster numbers.

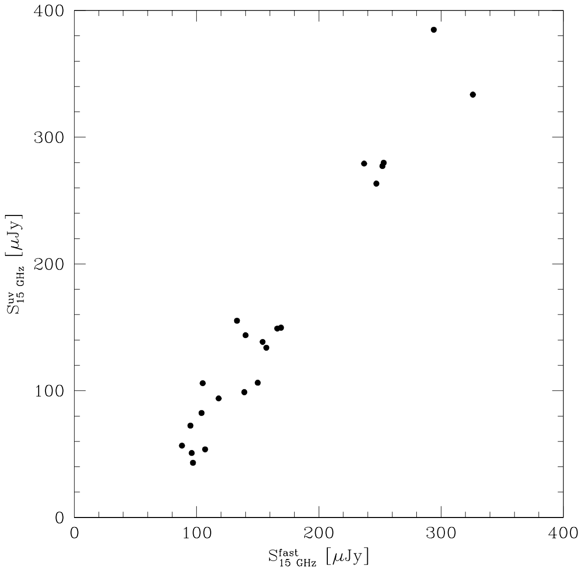

Figure 7. Comparison between the two algorithms simulating AMI observations; the fast algorithm on the horizontal axis against the detailed simulation of a small field on the vertical axis. Both methods estimate the recovered cluster flux sufficiently accurately for our purpose of evaluating the prospects of cluster detection, and we are not addressing here the issue of the final flux accuracy in the survey.

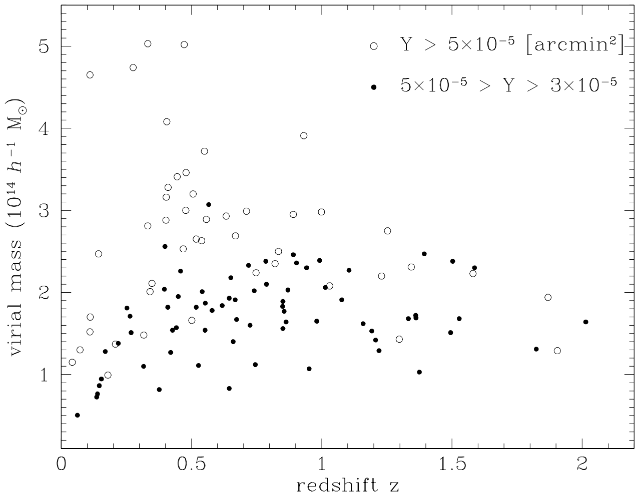

Figure 8. Masses and redshifts of the clusters detectable in the AMI survey in the $\Omega = 0.3$ cosmology. The AMI flux limit corresponds to an almost constant mass limit over all redshifts. The (arbitrary) flux binning demonstrates the advantage of a deep survey in finding high redshift clusters.

sumptions about σ_8 and f_g, or several hundred clusters for more realistic assumptions. The SZ cluster catalogue and the differential cluster counts at different flux levels will be prime observational results from the AMI blank field survey. Figure 8 shows the mass–redshift distribution we expect for the catalogued clusters in a $\Omega_0 = 0.3$ cosmology. The plot demonstrates that the sample is nearly mass-limited and that in a deep survey, which AMI can provide, many high redshift clusters can be found. This observational result, the cluster catalogue, needs to be interpreted in the framework of a model of cluster evolution. In our model, degeneracies exist between the input parameters for the observed cluster counts. Assuming prior errors on the input parameters as given in Table 2, a distinction between the two cosmologies or a reliable determination of Ω_0 is only marginally possible. Note however that the uncertainty in σ_8 comes mainly from the uncertainty in the mass–temperture conversion when inferring σ_8 from the cluster temperature function. For our purposes in predicting a mass $\times$ temperature function the uncertainty given in the Table can be seen as an upper limit. Extreme values for the individual parameters will already be severely constrained by the observation. At AMI sensitivities of $r_d^{-2} \int y \, \mathrm{d}A = Y \approx 4 \times 10^{-5}$ arcmin^2, the expected change in cluster counts due to changing the matter density is $N(\Omega_0 = 0.3)/N(\Omega_0 = 1) \approx 3.5$. In Figure 9 we show the parameter degeneracy as a function of the flux limit, and note that the matter density is better determined by cluster counts the deeper the observation is, because the slope of the counts is a function of the matter density as well. The Planck Surveyor, for example, is complementary to AMI in probing the counts at a higher flux limit of about 3–7 $\times 10^{-4}$ arcmin^2, where the cluster counts are mainly determined by σ_8, and the gas fraction. The slope of the cluster counts mea-

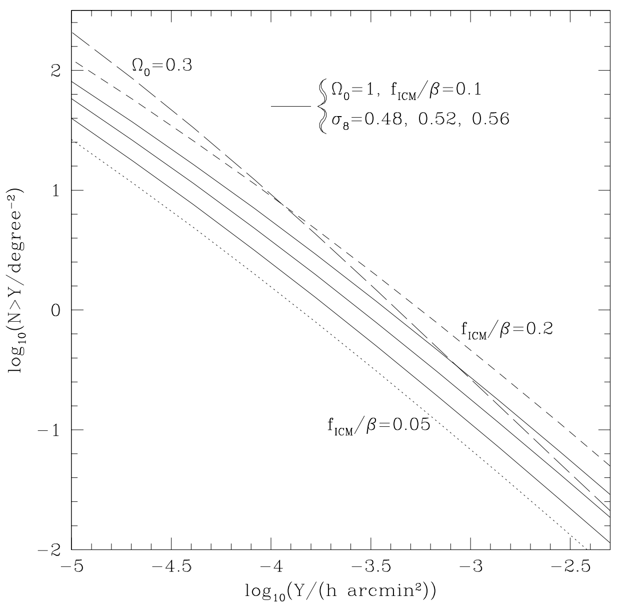

Figure 9. Cumulative source counts above a given integrated SZ effect, Y. The three solid lines illustrate the effect of varying the power spectrum normalisation, short-dashed and dotted lines show how the counts vary with increasing and decreasing gas fraction, and the long-dashed line is the default σ_8 and f_{ICM}/β prediction for the $\Omega_0 = 0.3$ model.

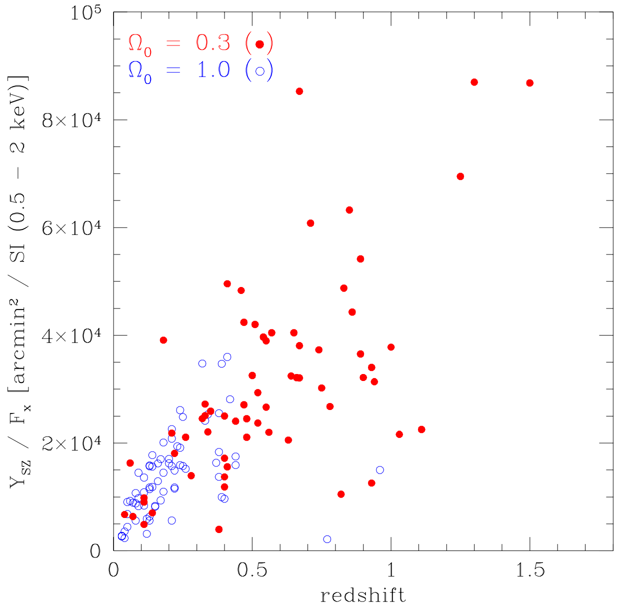

Figure 10. The ratio between SZ and X-ray flux (taken with a large aperture comparable to the virial radius for most clusters) is redshift dependent, "photometric" redshift; details in the text.

Parameter	change in percent	fractional change in $N(>Y)$
h	20 %	1.3
f_g	30 %	1.5
σ_8	7 % ($\sim 1\ \sigma$)	1.5
	14 % ($\sim 2\ \sigma$)	3.2

Table 2. The change in cluster counts by varying the model parameters.

sured over a wide range and to low fluxes would give direct evidence of the value of Ω_0.

In practice however, even with deep surveys the confusion between parameters remains unsatisfactory, but can be broken easily with basic follow-up observations in optical and X-ray wavebands, as we detail in the next section.

5.2 Basic X-ray and optical follow-up

Measuring redshifts optically and using the X-ray to Y flux ratios to identify the high redshift clusters (cf. Figure 10) will allow an estimate of the cluster space density as a function of the thermal energy, which is almost the mass, and of the redshift. The redshift distribution, crudely speaking, depends on Ω_0 and cluster physics affecting the gas fraction and the temperature both as a function of redshift. In Figure 11 we demonstrate the discriminative power of a statistical measure based on the redshift distribution, in this case the median, to distinguish values of Ω_0 even for a small cluster sample and incomplete follow-up, as long as redshift limits exist for half of the sample. The statistical analysis can be refined with better data to the point where a direct fit to the redshift data is possible, and tests of the very assumptions underlying our model can be carried out, i.e. for Gaussian initial conditions, gravitational collapse and various cluster physics effects neglected in the hydro-simulations. In Figure 12 we show that the redshift distribution is a much more robust estimator for the Ω_0 than the cluster counts, affected only by variations in the other model parameters larger than their presumed uncertainties.

With X-ray observations in particular we will get better determined cluster positions, the X-ray structure, indications of the gas temperature from hardness ratios and in a few cases redshifts via the iron-K line. The ratio of Y to X-ray flux (see Figure 10), directly proportional to the cooling time of a cluster at a given redshift, is also an indicator of the cluster redshift, due to the dimming of the X-ray flux, and the accuracy increases with redshift, in contrast to optical methods. With the scaling relations we have used to produce the sky maps (equations 2 and 3), we expect a scaling

$$\frac{Y}{F_x} \propto h\, f_g\, \beta^{-1}\, T^{-1/2}\, (1+z)^{5/2} \left(\frac{\Omega_0}{\Omega(z)}\right)^{-1/2} \left(\frac{\Delta_c}{178}\right)^{-1/2} . \quad (4)$$

The temperature dependence reflects that of the cooling function, is weak, and disappears when lowering the assumed power index of our non-evolving $L_x - T$ relation from 3 to 2, i.e. the value expected from simple scaling arguments. The last three factors in the above relation are all of cosmological relevance. The separation between the two cosmological models comes mainly from the redshift term, due to the different underlying redshift distributions, but also the other two terms give small additional factors greater than 1 for $\Omega_0 < 1$. Once the redshifts are known for all clusters, the relation can be used to determine $f_g \beta^{-1}$ statistically as a function of redshift for the sample.

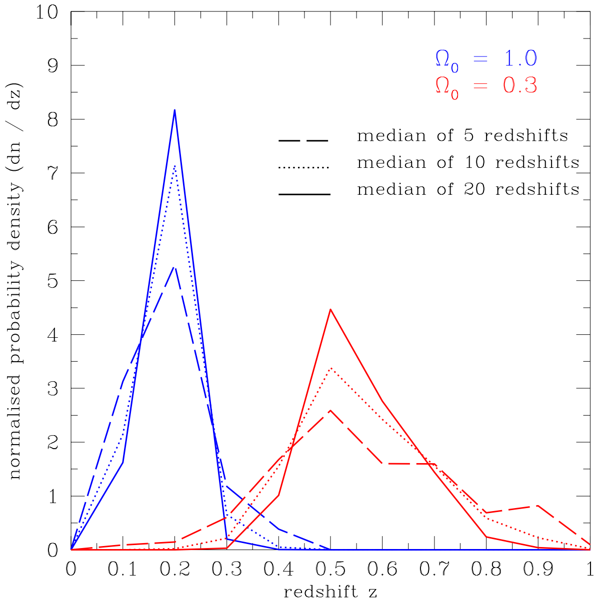

Figure 11. The distributions of median redshifts for the clusters detected by AMI separate the two cosmologies better with increasing sample size. However when redshifts are measured for only half of the clusters of a sample of only 20 clusters and lower limits exist for the other clusters, then there is a 90 % chance that one of the two cosmologies can be ruled out with >99.9 % confidence.

Our X-ray images (Figure 3) show a flux limit comparable to the sensitivity for future medium-deep surveys, for example with XMM, and no confusing X-ray background has been added. The number of clusters detectable in X-rays is large, but the sample is strongly biased towards nearby less massive clusters. Therefore no obvious difference between the two cosmologies is apparent in the X-ray maps. A comparison of the redshift distributions is shown in Figure 13. The redshift distributions of the observed clusters separate clearly with matter density for the AMI samples, but do so only at a very low flux limit and only for a very large number of clusters in the X-rays. To find high redshift clusters efficiently and to probe cosmology, deep SZ surveys have a clear advantage. However X-ray follow-up on SZ-selected clusters is also important to exploit the information which becomes accessible with such an SZ survey, for example to separate gas density and temperature. The present (and future) X-ray telescopes with high resolution, high sensitivity, but small fields of view are ideal for this purpose. The exposure time per cluster ideally would be matched to ensure a similar number of X-ray counts per cluster in the sample to study it in a largely redshift-independent way.

Therefore combining all the information from the blank field SZ survey, X-ray and optical follow-up promises a determination of all the model parameters individually, assuming that real clusters are similar enough to our simulated ones. The AMI sample can be studied further in many ways and compared to other probes of cosmology, which would identify cluster physical effects which we have neglected and therefore improve the understanding of cluster formation and evolution.

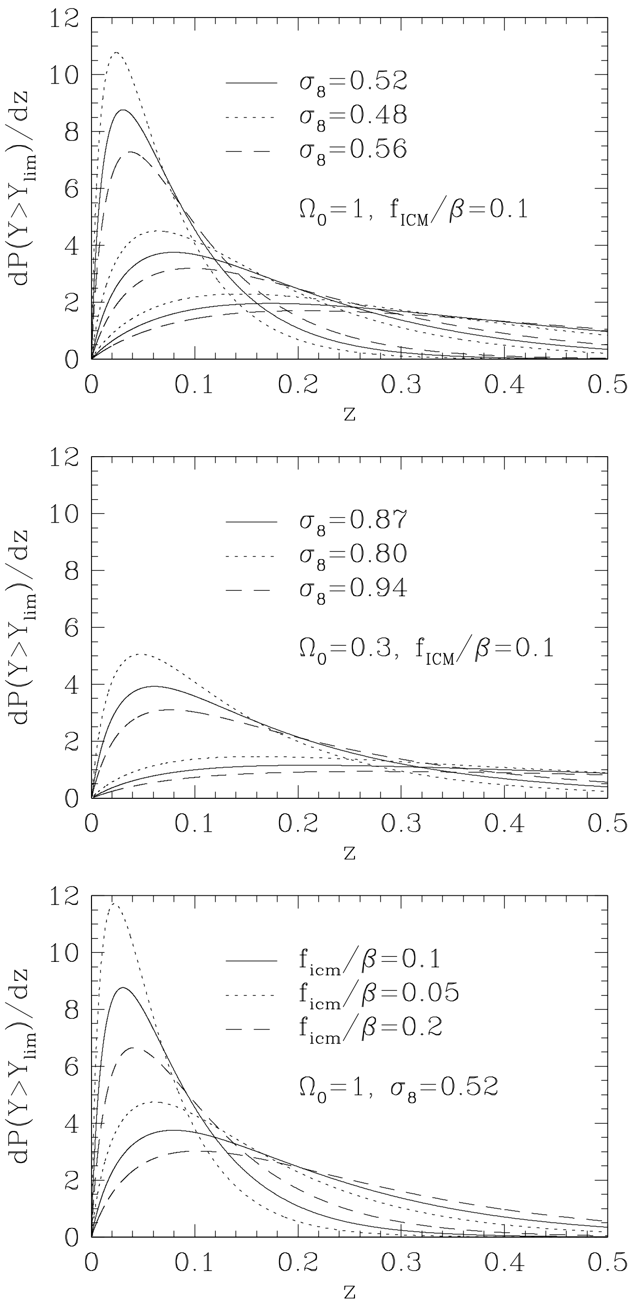

Figure 12. Redshift distributions for the model cluster distributions assuming various different model parameters. The top panel shows the effect of varying the power spectrum normalisation σ_8 for the $\Omega_0 = 1$ model with the default value of f_{ICM}/β. The three different sets of curves correspond to different limiting cluster Y values of $10^{-3}, 10^{-4}$ and 10^{-5} h arcmin^2 going from most peaked to most extended redshift distribution respectively. The middle panel shows the corresponding figure for the $\Omega_0 = 0.3$ model. Only the $Y_{lim} = 10^{-3}$ and 10^{-4} cases are shown, with the fainter clusters being even more extended. The bottom panel shows how the redshift distribution changes with f_{ICM}/β for the cluster normalised $\Omega_0 = 1$ model. Again, only the $Y_{lim} = 10^{-3}$ and 10^{-4} cases are plotted.

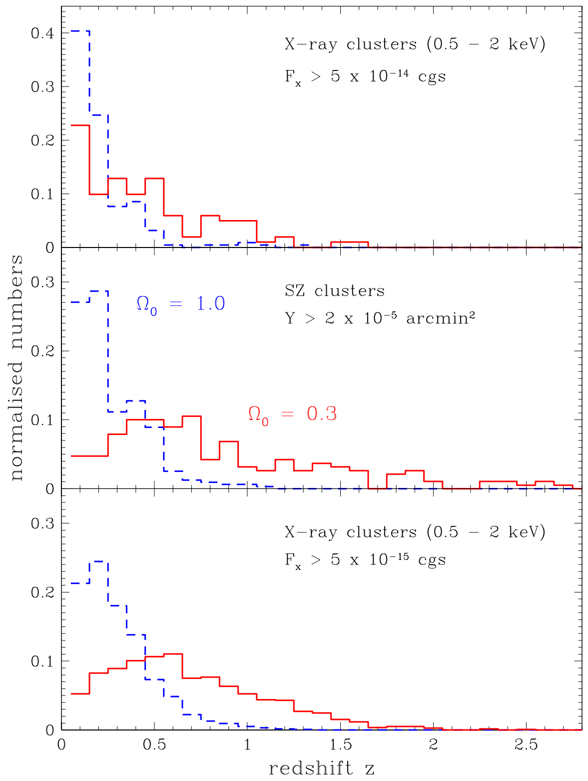

Figure 13. Comparison of the redshift distributions for cluster samples selected from SZ and X-ray observations. The depth in X-ray flux in the top panel is a factor of two below current flux limits in medium sized surveys and returns of the order of 4 clusters per square degree, a number similar to the SZ case (centre panel). However to distinguish the cosmologies comparable to the SZ case another factor of 10 deeper (bottom panel) is required. Even at this low flux limit the X-ray selection process returns relatively fewer clusters at very high redshifts than the SZ observation. Note the near completeness in all samples for the $\Omega_0 = 1$ case.

5.3 Detailed AMI, X-ray, optical and other follow-up

The following observations could be carried out to provide a detailed study of the AMI cluster sample:

- sensitive, high resolution images from AMI in non-survey mode (see Figure 14);
- X-ray temperature maps;
- total projected mass from gravitational lensing; and
- SZ observations at frequencies above 217 GHz.

We expect that the following results, all as a function of redshift, can be achieved:

- gas and temperature structure: basic shapes, merging, cooling, structure changes over time;
- investigation of the virialisation state through SZ and lensing observations;
- testing the temperature–mass relation and preheating;
- comparing gas and dark matter (f_g) structures (note that the sensitive SZ measurements, which measure the gas mass directly (as long as the temperature distribution is understood), would be a better probe of the gas fraction than X-ray measurements, which give the gas mass in a model-dependent way from the emission measure, which is proportional to the square of the density);
- cluster peculiar velocities (kinematic SZ effect);
- effects of the (temperature-dependent) relativistic tail and non-thermal effects of the electron gas; and
- determination of galaxy masses and types.

In particular all the data would be available to determine the angular distance r_d to the clusters (Gunn 1978; Silk & White 1978; Cavaliere, Danese and De Zotti 1979; Birkinshaw 1979), and therefore with the redshifts $H(z)$ or to low order H_0 and q_0 (which depends on Ω_0 and Ω_Λ) can be estimated. This absolute distance method is independent of cluster evolution and works in principle for an individual cluster, as long as the parameters entering the relation for r_d can be measured reliably and the cluster gas and temperature distributions can be modelled sufficiently accurately. We know there are uncertainties in this modelling process, for example through clumping, cooling, or temperature gradients. But we have found, from analytic modelling and the hydrodynamical simulation templates, that the effects on estimating H_0 and q_0 tend to cancel out even for a single cluster, and certainly for a larger sample (Grainger et al.). In a low density universe ($\Omega_0 = 0.3$) where many clusters, are expected at high redshifts, the AMI sample contains an about equal number of clusters below and above $z = 0.5$. For simplicity we divide the sample into one at $z = 0$ which determines H_0 and one at $z = 0.8$ which in comparison determines q_0. To achieve an accuracy of about 5 % in the angular distance relation, which is at least comparable to the supernovae results (Riess et al. 1998; Perlmutter et al. 1999), we will need samples of 30 clusters each at low and high redshift, mainly to reduce the effect of unknown orientation. A different and source evolution independent method to constrain the cosmological constant seems in sight.

6 CONCLUSIONS

Technological advances now allow a detailed study of cluster gas in SZ for individual bright clusters and a blank field survey to search for fainter clusters. Both aspects are of great relevance for understanding the formation and evolution of clusters and their gas content in a cosmological context. The SZ effect probes the product of gas mass and temperature directly and almost independently of redshift.

We have shown:

(i) We have assessed the performance in finding clusters of the proposed interferometer array AMI with realistic SZ sky simulations and detailed simulations of the observing process. With very conservative assumptions about gas fractions and the power spectrum amplitude, AMI will discover 20 ($\Omega_0 = 1$) to 70 ($\Omega_0 = 0.3$) clusters with total mass $\geq 10^{14}$ $M_\odot$ per year, and several hundred under more realistic assumptions, many beyond redshift one.

(ii) The cluster sample will constrain a combination of key cosmological parameters and the process of structure formation. The cluster survey will permit optical and X-ray follow-up to measure individual parameters, such as the mean matter density, the power spectrum amplitude, and

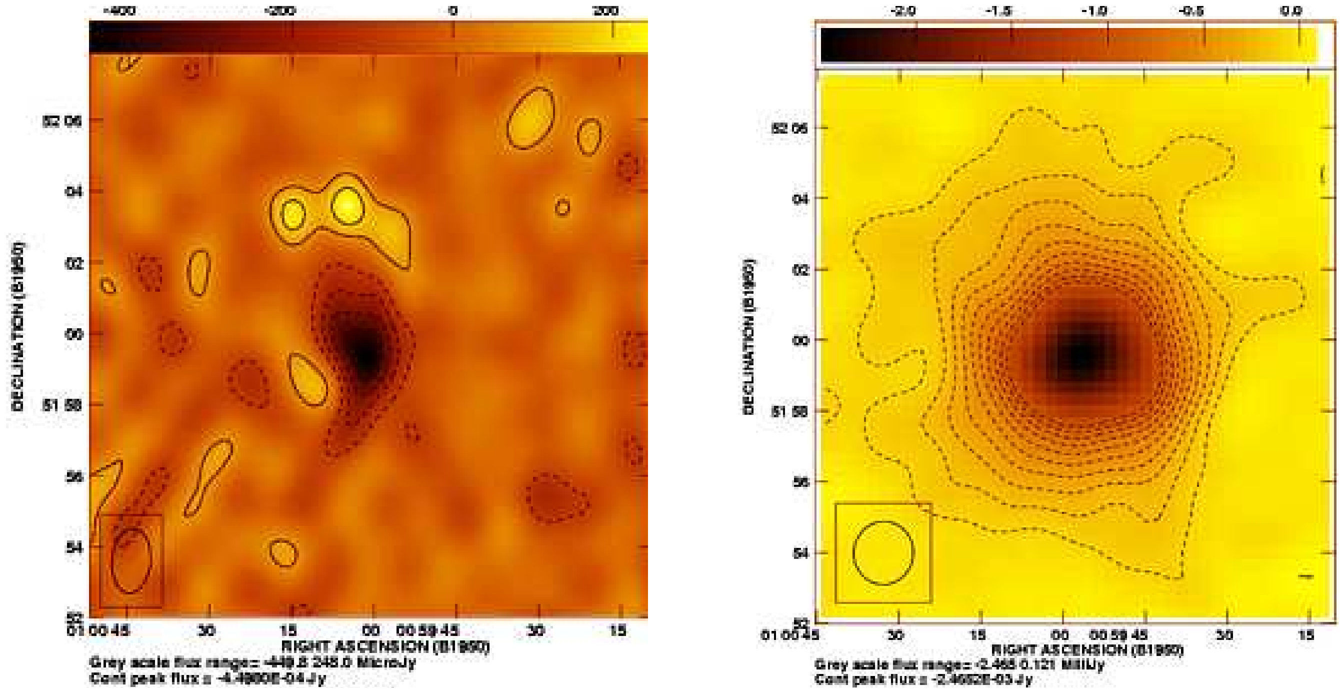

Figure 14. Left: An image of 84 hours of RT data showing an SZ effect in Abell 1914 which is essentially unresolved. Right: A simulated observation of the cluster with AMI of the same integration time. The spatial dynamic range and signal-to-noise ratio are vastly increased, providing detailed structural information on the cluster gas; indeed no structure due to receiver noise is visible in the background.

gas density and temperature structures and their evolution, to good approximation. Selecting clusters from a deep SZ survey also provides for a very efficient use of X-ray observation time. Those at high redshift will be key targets for multi-waveband studies of cluster evolution.

(iii) Because the survey method provides a sample of high redshift clusters that is essentially selected by mass it will be possible to make reliable distance estimates at high redshift and hence measure q_0.

(iv) Such an instrument will also be able to make highly detailed pointed observations of clusters.

ACKNOWLEDGMENTS

RK acknowledges support from an EU Marie Curie Fellowship. VRE and CG acknowledge support from PPARC Postdoctoral Fellowships.

REFERENCES

Barbosa D., Bartlett J.G., Blanchard A., Oukbir J., 1996, A&A, 314, 13
Birkinshaw M., 1979, MNRAS, 187, 487
Birkinshaw M., 1999, Phys. Rept., 310, 97
Birkinshaw M., Gull S.F., Hardebeck H., 1984, 309, 34-35
Bardeen J.M., Bond J.R., Kaiser N., Szalay A.S., 1986, ApJ, 304, 15
Bartlett J.G., Silk J., 1994, ApJ 423, 12
Bartlett J.G., A&A, submitted, (astro-ph/0001267)
Bond J.R. & Meyers S.T. 1991, in: Trends in Astroparticle Physics, ed. D. Cline, World Scientific, Singapore
Bryan G.L., Norman M.L., 1998, ApJ, 495, 80
Carlstrom J. E., Joy M., Grego L., 1996, ApJL, 461, L59
Carlstrom J.E., Joy M., Grego L., 1996, ApJ 456, L75
Cavaliere A., Danese L. and De Zotti G., 1979, A&A, 75, 322
Church, S.E., 1995, MNRAS, 272, 551
Cotter et al., MNRAS submitted
Colafrancesco S., Mazzotta P., Rephaeli Y., Vittorio N., 1997, ApJ, 433, 454
da Silva, A.C., Barbosa, D., Liddle, A.R., Thomas, P.A., 2000, MNRAS 317, 37
Della Ceca R., Scaramella R., Gioia I.M., Rosati P., Fiore F., Squires G., 2000, A&A, 353, 498
Donahue M., Voit G.M., Scharf C.A., Gioia I.M., Mullis C.R., Hughes J.P., Stocke J.T., 1999, ApJ, 527, 525
Gunn J.E., 1978, in: Observational Cosmology, ed. A. Maeder, L. Martinet and G. Tammann (Geneva: Geneva Observatory)
Fabian A.C., Crawford C.S., Ettori S., Sanders J.S., 2001, MNRAS in press (astro-ph/0101478)
Eke, V. R., Cole, S., & Frenk, C. S. 1996, MNRAS, 282, 263
Eke V.R., Navarro J.F., Frenk C.S., 1998, ApJ 503, 569
Ettori S., Fabian A.C., 1999, MNRAS 305, 834
Ettori S., Allen S.W., Fabian A.C., 2001, MNRAS in press (astro-ph/0010162)
Grainge, K., Jones, M., Pooley, G., Saunders, R., & Edge, A. 1993, MNRAS, 265, L57
Grainge, K., Jones, M., Pooley, G., Saunders, R., Baker, J., Haynes, T., & Edge, A. 1996, MNRAS, 278, L17
Grainger W., et al., in preparation
Haiman Z., Mohr J.J., Holder G.P., ApJ, submitted, (astro-ph/0002336)
Holder G.P., Mohr J.J., Carlstrom J.E., Evrard A.E., Leitch E.M., 2000, ApJ, 544, 629
Holzapfel, W. L., Wilbanks T. M., Ade P. A. R., Church S. E., Fischer M. L., Mauskopf P. D., Osgood D. E., Lange A. E.,

1997, ApJ, 479, 17
Jones, M., et al. 1993, Nature, 365, 320
Joy M., LaRoque S., Grego L., Carlstrom J.E., Dawson K., Ebeling H., Holzapfel W.L., Nagai D., Reese E.D., ApJL submitted, (astro-ph/0012052)
Kneissl, R., 2000, in: Large Scale Structure in the X-ray Universe, eds. Plionis, M. & Georgantopoulos, I., Atlantisciences, France, 185 (astro-ph/0001106)
Korolev V.A., Sunyaev R.A., Yakubtsev L.A., 1986, Sov. Astron. Lett. 12, 141
Lay, O.P., Halverson N.W., 2000, ApJ, 543, 787
Lo, K.Y., Chiueh T.H., Martin R.N., Ng K.-W., Liang H., Pen U.-I., Ma Ch.-P., in: "New Cosmological Data and the Values of the Fundamental Parameters", IAU Symposium 201, eds. A.N. Lasenby and A. Wilkinson, (astro-ph/0012282)
Markevitch M., Blumenthal G.R., Forman W., Jones C., Sunyaev R.A., 1994, ApJ, 426, 1
Matarrese S., Verde L., Jimenez R., 2000, ApJ, 541, 10
Mohr J.J.,Mathiesen B., Evrard A.E., 1999, ApJ 517, 627
Myers S.T., Baker J.E., Readhead A.C.S., Leitch E.M., Herbig T., 1997, ApJ, 485, 1
Perlmutter S., et al., 1999, ApJ, 517, 565
Press W.H., Schechter P., 1974, ApJ 187, 425
Riess A.G., et al., 1998, AJ, 116, 1009
Scheuer P.A.G., 1957, Proc. Camb. Phil. Soc., 53, 764
Schindler S., 1999, A&A, 349, 435
Silk J., White S.D.M., 1978, ApJL, 226, L103
Sunyaev R.A., Zel'dovich Ya., 1972, Comments Astrophys. Space Phys. 4, 173
Taylor A.C., Grainge K., Jones M.E., Pooley G.G., Saunders R., Waldram E.M., MNRAS, submitted
Interferometry and synthesis in radio astronomy, Thompson, A. R., Moran, J. M., Swenson, G. W., 1986, Wiley
Tytler D., O'Meara J.M., Suzuki N., Lubin D., 2000, Physica Scripta, 85, 12
Wang L., Steinhardt P.J., 1998, ApJ, 508, 483
White S.D.M., Navarro J.F., Evrard A.E., Frenk C.S., 1993, Nature, 366, 429
Windhorst R. A., Fomalont E.B., Partridge R.B., Lowenthal J.D., 1993, ApJ, 405, 498

This paper has been produced using the Royal Astronomical Society/Blackwell Science LaTeX style file.